Polarized light metrology for thin-film photovoltaics: research and development scale processes

R.W. Collins[1], **Jian Li** [2], **Michelle N. Sestak**[1] & **Sylvain Marsillac**[3],
[1]Center for Photovoltaics Innovation & Commercialization and Department of Physics & Astronomy, University of Toledo, Ohio; [2]National Renewable Energy Laboratory, Golden, Colorado, and Department of Electrical Engineering & Computer Science, University of Michigan, Ann Arbor, Michigan; [3]Department of Electrical & Computer Engineering, Old Dominion University, Norfolk, Virginia, USA

ABSTRACT

Optical probes based on polarized light spectroscopy, including spectroscopic ellipsometry (SE) and polarimetry, have been applied in research and process development for the three major thin-film photovoltaics technologies, including thin-film hydrogenated silicon (Si:H), cadmium telluride (CdTe), and copper indium-gallium diselenide (CuIn$_{1-x}$Ga$_x$Se$_2$). Real-time SE during materials fabrication has provided insights into the nucleation, coalescence, and structural evolution of these thin films. These insights have led, in turn, to guiding principles for PV performance optimization, as well as future directions for real-time process control. The optical properties deduced simultaneously with the layer thicknesses using real-time SE have been applied to characterize the phase composition of materials (amorphous versus crystalline), the mean free path and grain size, and the relative free carrier concentration. As a result, analytical formulae for the optical properties of PV materials have been developed with free parameters that are linked to basic materials properties. This paper shows how the formulae and associated parameter-property relationships can serve as a database for analyzing complete PV stacks, with future prospects for mapping layer thicknesses and basic materials properties in on-line monitoring applications for large-area PV plates and modules.

Introduction

Non-destructive and non-invasive measurement and monitoring tools are needed at all stages of thin-film photovoltaics development; in research laboratories, in scale-up of processes, and in production [1, 2]. Maturation of thin-film technologies has led to a growing demand for such probes particularly for on-line monitoring and control of manufacturing lines. Depending on the technology, optimized thin-film PV device fabrication may require the deposition of a dozen or more major layers, with the possibility of additional intentionally-graded and inadvertent transition layers between major layers. Some transition layers may be as thin as a few atomic distances, or one nanometer (nm), and the major layers may be as thick as 10 microns (μm). Substrates on which these multilayers are fabricated can range in size from cm^2 or less for specialized substrates – designed for exceptional crystalline quality in thin film form – to m^2 for glass plates, designed for low cost production of amorphous, nanocrystalline, or polycrystalline thin films. As a result, in thin-film PV the thickness *d* for each layer and its uniformity over the substrate area collectively represent a critically-important starting point in the evaluation of the overall performance of the multilayer PV stack.

At the next level of detail in component layer evaluation, the spectral dependence of the index of refraction and extinction coefficient (*n*, *k*) and their uniformity are also critically important, as these spectra, in conjunction with the set of *d*, enable the calculation of the internal quantum efficiency (QE) of the PV device at a given location on its surface. The internal QE describes the number of electron-hole pairs generated within the active material component of the device per unit area per unit time – given as a ratio of the incident photon flux. The differences between the calculated internal QE and the measured QE provide insights into the spectral dependence of electronic losses. Further analysis of the deduced (*n*, *k*) spectra can also yield more fundamental optical parameters of critical point (CP) amplitudes, CP energies or bandgaps and CP widths. These can provide information on material density, temperature, composition, strain, grain size, and defect density, assuming that the appropriate parameter-property relationships are established.

> “Polarized light spectroscopies have served as non-invasive optical probes of thin films and multilayers in a wide variety of technologies.”

In this article, the application of polarized light spectroscopy will be described for the determination of thicknesses and (*n*, *k*) spectra toward the analysis and optimization of PV fabrication processes on the research and development scale. Polarized light spectroscopies, which encompass ellipsometry and polarimetry – both performed in reflection – have served as non-invasive optical probes of thin films and multilayers in a wide variety of technologies (see Fig. 1) [3-7]. Polarized light spectroscopies achieve a significant advantage over reflectometry through the additional measurement of a phase difference. Reflectometry exploits the change in real irradiance *I* upon reflection; however, the technique of ellipsometry exploits the change in a complex polarization state parameter ξ, which includes both a relative amplitude |ξ| and a phase difference δ: $\xi = |\xi|\exp(i\delta)$ [3]. In turn, the relative amplitude |ξ| is the ratio of two orthogonally-directed, linearly-polarized optical field amplitudes, and δ is the phase difference between the two orthogonal components. The irradiance change upon reflection is characterized by the reflectance $R = I_r/I_i$, the ratio of the reflected (*r*) to incident (*i*) beam irradiances, whereas the polarization state change is defined analogously, but as a complex number $\rho = \xi_r/\xi_i = (|\xi_r|/|\xi_i|)\exp\{i(\delta_r - \delta_i)\}$.

Thus, ellipsometry provides two angles, one defined (historically) in terms of a ratio of the relative amplitudes |ξ| by $\psi = \tan^{-1}(|\xi_r|/|\xi_i|)$, and the second described as a shift (upon reflection) in the phase difference δ given by $\Delta = \delta_r - \delta_i$ [3]. Ellipsometry is less sensitive to surface defects and macroscopic roughness that may scatter power out of the optical beam because, ultimately, it is based on the measurement of the shape (not the size) of the polarization ellipse – characterized by tilt and ellipticity angles (Q, χ). It can also be made less sensitive to small variations in alignment that would require recalibration in a reflectance experiment. The ellipsometry angle Δ exhibits extraordinary sensitivity to film thickness. High precision ellipsometers can detect the formation of fractions of a monolayer, 0.01nm in effective thickness, while providing the (n, k) spectra for thin films at the level of a few monolayers [8].

Applications in the three major thin-film technologies of hydrogenated amorphous and nanocrystalline silicon [a-Si:H and nc-Si:H], cadmium telluride [CdTe], and copper indium-gallium diselenide [$Cu(In_{1-x}Ga_x)Se_2$, or CIGS] will be described at research and development scales. In some cases, detailed insights into process optimization have been obtained; in others, a foundation for in-depth process development is being established. A second goal of the R&D scale activity is the development of an optical property or (n, k) database including analytical formulas and associated parameter-property relationships for all the major thin-film PV materials, from metallic and transparent conducting oxide contacts to the *n*-type, *p*-type, and intrinsic semiconductors [9]. Such a database is particularly useful for on-line and off-line analysis of materials on a manufacturing scale. A description of these analysis efforts is beyond the scope of the present article.

Polarized light measurements

Spectroscopic ellipsometry

The simplest ellipsometry measurement is that of a bare isotropic substrate, or its optical equivalent, an opaque ideal, isotropic thin film. If the dielectric function ε_a of the ambient medium (typically air or vacuum) and the oblique angle of incidence θ_i are both known, then (ψ, Δ), as defined in the previous section, provide directly the real and imaginary parts $(\varepsilon_{1s}, \varepsilon_{2s})$ of the complex dielectric function of the substrate (or opaque film) for the given optical wavelength λ of measurement (or photon energy of measurement: $E = hc/\lambda$; where c is speed of light and h is Planck's constant) [3]. The complex dielectric function of the substrate $\varepsilon_s = \varepsilon_{1s} + i\varepsilon_{2s}$ is obtained from its complex index of refraction $N_s = n_s + ik_s$, simply according to $\varepsilon_s = N_s^2$, so that $\varepsilon_{1s} = n_s^2 - k_s^2$ and $\varepsilon_{2s} = 2n_sk_s$, where (n_s, k_s) are the index of refraction and extinction coefficient of the substrate, respectively. For a non-absorbing ambient medium, $k_a = 0$ and so $\varepsilon_{1a} = n_a^2$ and $\varepsilon_{2a} = 0$. This measurement capability provides the unique opportunity for spectroscopic ellipsometry to measure directly the wavelength or photon energy $(E=\hbar\omega)$ dependence of the complete optical properties of a substrate or an opaque film, either in the form of ε_s or N_s. Thus, spectroscopic ellipsometry enables development of a reference set of material dielectric functions [9] that can then be applied to assist in the analysis of ellipsometry data on single thin films and multilayers.

> "Spectroscopic ellipsometry enables development of a reference set of material dielectric functions."

The next step in the progression of ellipsometric measurement and analysis involves determination of the thickness d and the real and imaginary parts of the complex dielectric function $(\varepsilon_{1f}, \varepsilon_{2f})$ of a single unknown, ideal, isotropic thin film on a known isotropic substrate. Because there are three unknowns: $\{d, (\varepsilon_{1f}, \varepsilon_{2f})\}$, in a single photon energy problem and only two data values: (ψ, Δ), then multiple measurements are required [3]. As spectroscopic ellipsometry is powerful in its own right (as described in the next paragraph), this same multiple measurement approach is also the most desirable for solving the single film data analysis problem. For spectra consisting of M photon energies, there are $2M + 1$ unknown parameters, including M pairs of $(\varepsilon_{1f}, \varepsilon_{2f})$ as well as one d value, but only $2M$ measured (ψ, Δ) values. In spite of this, it is still possible to solve the single film problem using a single pair of (ψ, Δ) spectra, in a process called artifact minimization [10]. Even greater success results, however, from measuring and analyzing multiple spectra at different times during film growth, through the methods of real-time spectroscopic ellipsometry [11]. If spectra with M photon energies are collected at N different times, associated with different values of d during deposition of a film with a constant dielectric function versus d, then there are $2M + N$ unknowns and $2MN$ data values. For typical values used in real time spectroscopic ellipsometry, with state of the art instrumentation, M and N are each on the order of 10^2 – 10^3, and the analysis solution is greatly over-determined.

The dielectric function $(\varepsilon_1, \varepsilon_2)$ of a substrate or thin film, versus photon energy, can be described as an analytical function of lineshape parameters, including amplitudes A_n, energies E_n, and broadening parameters Γ_n, which provide information on physical characteristics [12,13]. For example, A_n reflects material density; E_n reflects material temperature, composition, and strain; and Γ_n reflects defect density, grain size or ordering, depending on the structure (crystalline, polycrystalline, or amorphous, respectively). In many cases, such information cannot be determined directly and must be established through correlations of optical data with direct measurements that enable development of parameter-property relationships. If ε_f can be expressed accurately as an analytical function of lineshape parameters, then the single film analysis problem can be reduced to least-squares regression or determination of only $\hbar\omega$-independent parameters. The validity of the best-fit model for $(\varepsilon_{1f}, \varepsilon_{2f})$ is evaluated using the mean square error between the best-fit simulation and the experimental (ψ, Δ) spectra [14].

A single thin film on a substrate can rarely be modelled adequately assuming a single layer between the semi-infinite ambient and substrate. Film surfaces and interfaces are microscopically rough to at least some degree, with possible film/substrate interdiffusion as well. Microscopic roughness, i.e., roughness having an in-plane scale much smaller than the light wavelength, can be incorporated into the optical model as one or more layers. The complex dielectric functions of these layers are modelled assuming effective media of the underlying and overlying materials. The Bruggeman approximation has been applied most widely for determining ε for microscopic mixtures based on the dielectric functions and volume fractions of the components [15,16]. Consequently, roughness regions can be incorporated into least squares regression through the addition of $\hbar\omega$-independent thickness parameters [14].

> "A single thin film on a substrate can rarely be modelled adequately assuming a single layer between the semi-infinite ambient and substrate."

The final step in the progression of ellipsometric measurement and analysis capability involves characterization of a full multilayer stack [3,14]. In this case, a single pair of (ψ, Δ) spectra can be useful under two circumstances. First, if all dielectric functions in the problem are known, or if some are known and others can be expressed in terms of a few wavelength independent lineshape parameters [e.g., (A_n, E_n, Γ_n)], then least-squares regression can provide the thicknesses of the bulk, surface roughness and interface roughness layers as well as the dielectric function parameters. Second, if only one dielectric function is unknown and one to three thicknesses are unknown, then the artifact minimization method is possible. The best solution, however, is real-time

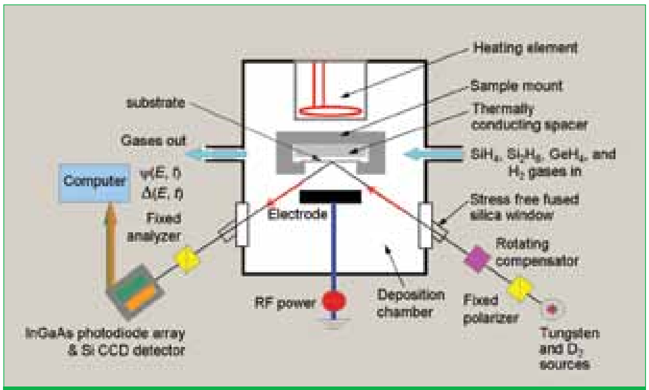

Figure 1. Schematic of a commercially-available, rotating-compensator multichannel ellipsometer (J.A. Woollam Co., M2000-DI) integrated with a system for thin-film silicon preparation by plasma-enhanced chemical vapour deposition.

spectroscopic ellipsometry, which can overdetermine the thickness and optical properties of each layer as it is deposited. In such a case, very fine details of the film structure related to interactions with the substrate, surface roughness development, and even optical property evolution can be incorporated into the deposition models.

Spectroscopic polarimetry

The presence of a variety of non-idealities in thin-film structures motivates spectroscopic polarimetry. This technique involves generating an optical beam with a known four-component Stokes vector ($\mathbf{S}_i$), reflecting that beam from a surface, and detecting the four-component Stokes vector ($\mathbf{S}_r$) after reflection [17], such that both generation and detection are spectrally resolved and characterized. The Stokes vector describes not only the polarization ellipse shape (Q, χ), but also the beam irradiance I and degree of polarization p. Changes in the ellipse shape (Q, χ) upon reflection can provide the angles (ψ, Δ), as in ellipsometry. Changes in I upon reflection can provide information on macroscopic roughness, whose in-plane scale is on the order of the wavelength and scatters irradiance out of the beam. Finally, changes in p upon reflection can provide information on non-uniformities that lead to a distribution of thickness or optical properties over the probed area: typically 0.1 – 1cm^2. The non-uniformities in turn lead to a distribution of reflected beam polarization states, or depolarization of the incident polarized beam, yielding $p < 1$. By expanding spectroscopic polarimetry to the measurement of the sample's 4×4 Mueller matrix $\mathbf{M}_S$, which describes how the sample modifies any incident 4×1 Stokes vector upon reflection [17], anisotropic systems can be characterized – including the thicknesses and principal axis complex dielectric functions of substrates and films [14].

Applications of polarized light spectroscopy in photovoltaics

Applications of real-time spectroscopic ellipsometry (RTSE) in the three major thin-film photovoltaic technologies will now be discussed in order of maturity of the technology, which parallels the level to which the RTSE capability has been advanced in each case. For thin-film hydrogenated silicon (Si:H), significant progress has been made in understanding the growth mechanisms using RTSE, and in developing guiding principles for the optimization of both amorphous silicon (a-Si:H) and nanocrystalline silicon (nc-Si:H) solar cells [18]. For thin-film CdTe, RTSE studies currently explore the relationships between the nucleation and growth dynamics of as-deposited CdTe and CdS and the resulting solar cell performance, and the ability of the dielectric functions to provide information on temperature, strain and grain size in these materials [19]. In this case, the complexity of such relationships is enhanced as a result of the post-deposition $CdCl_2$ treatment. Finally, for CIGS, RTSE studies are at an early stage, and the initial effort requires developing dielectric function database

components of the relevant phases and compositions of the materials.

Fig. 1 shows an apparatus used for real time spectroscopic ellipsometry in the rotating-compensator configuration. The commercial instrument shown here (J.A. Woollam Co., M2000-DI) consists of a broadband light source incorporating both D_2 and filament lamps for a spectral range of 0.75 to 6.5eV. A collimated light beam from the source passes through a polarizer and a continuously rotating compensator. Upon transmission of the beam, the compensator imposes a shift in the phase difference between two orthogonal linear polarization components, resolved along the fast and slow axes of the device, thus generating elliptically polarized light in general. The beam then passes through a strain-free window into the chamber, reflects from the growing film, and exits the chamber. After passing through the second strain-free window, the light is analyzed with a second polarizer and spectroscopically resolved and measured using a pair of linear array detectors. The deposition system shown schematically in Fig. 1 is designed for the fabrication of thin-film Si:H from silane or disilane and hydrogen gases by plasma-enhanced chemical vapour deposition (PECVD), although the same spectroscopic ellipsometer can also be mounted onto deposition systems used for CdTe and CIGS.

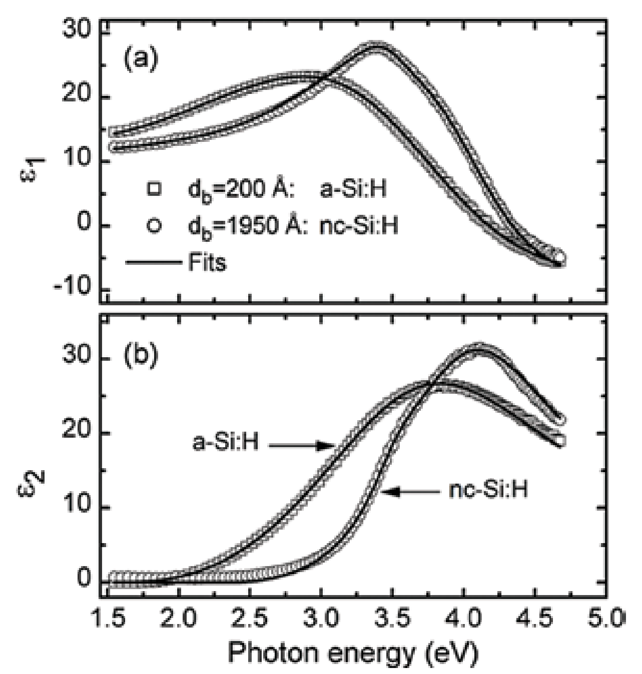

Figure 2. The real (a) and imaginary (b) parts of the dielectric functions of intrinsic amorphous and nanocrystalline Si:H (a-Si:H and nc-Si:H, respectively), measured at 200°C in RTSE studies of 20 and 195nm thick films (points). The solid line results have been calculated from oscillator models using best-fit lineshape parameters appropriate for a temperature of 200°C [21].

Thin-film hydrogenated silicon (Si:H)

Thin-film Si:H is the most extensively studied of the thin-film solar cell materials since it encompasses prototypical amorphous and nanocrystalline semiconductors [20]. The best small area solar cells from multijunctions of these materials exhibit a factor of two lower efficiency than the corresponding best c-Si solar cells. In spite of this, the thin-film Si:H does present certain advantages such as relaxed crystal momentum conservation (hence strong absorption for a much reduced thickness), abundant non-toxic materials, and a potential for low production costs [20]. The Si:H materials are deposited by plasma-enhanced chemical vapour deposition in low temperature processes (< 300°C) using SiH_4 or Si_2H_6 and H_2, making these solar cells excellent candidates for fabrication on flexible substrates in roll-to-roll processes. By altering the deposition parameters, most notably the R value (the ratio of H_2 to SiH_4 or Si_2H_6 gas flows), a thin Si:H film can be made amorphous, mixed-phase or nanocrystalline. These forms of thin-film Si:H have been studied in detail using RTSE [18, 21].

Fig. 2 compares the deduced dielectric functions of purely amorphous and purely nanocrystalline phases of Si:H (a-Si:H and nc-Si:H, respectively) measured at a calibrated substrate temperature of 200°C [21]. Although the overall shapes are similar, the nc-Si:H dielectric function shows two features near 3.4 and 4.2eV, which are the broadened critical points characteristic of crystal Si [22]. In contrast, the a-Si:H dielectric function shows a single, much broader feature due to complete loss of long-range order. This loss leads to a relaxation of crystal momentum (or electron **k**-vector) conservation and as a result, a larger imaginary part of the dielectric function is observed just above the band gap (1.8eV) for a-Si:H than for nc-Si:H. Thus, stronger absorption is obtained over much of the photon energy range of the visible spectrum, from 2 to 3eV. It is these differences that enable one to distinguish readily between the two phases and to characterize the evolution of mixed-phase materials using RTSE as shown in Fig. 3 [21].

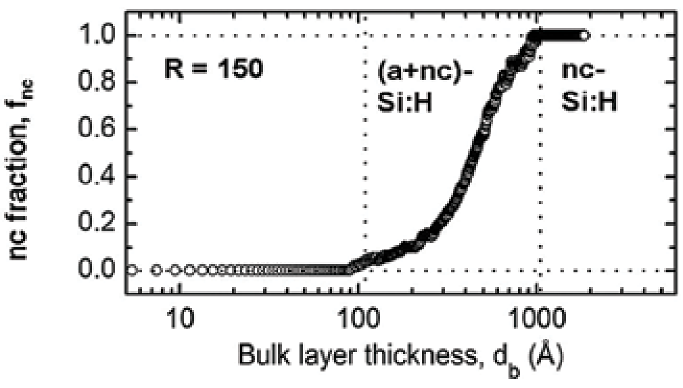

Figure 3. Depth profile in the nanocrystalline volume fraction (f_{nc}) from the substrate (left) to the surface (right) for a mixed-phase Si:H *i*-layer deposited under fixed conditions with a nominal substrate temperature of 200°C and *R*=150 on top of an a-Si:H *n*-layer [18].

Fig. 3 presents the RTSE-deduced depth profile of the volume fraction of nanocrystalline phase (f_{nc}) in a mixed-phase Si:H intrinsic layer (*i*-layer), obtained as the PECVD film evolves in thickness under fixed conditions: a nominal substrate temperature of 200°C and R = 150 [18]. RTSE can be used to calibrate the actual substrate temperature, and the result in this case (110°C) is considerably lower than the nominal value (200°C). The substrate is an a-Si:H *n*-layer film, which starts the layered configuration used for a standard amorphous *n-i-p* solar cell. The results of Fig. 3 are obtained by applying to the RTSE data the virtual interface analysis technique including a pseudo-substrate approximation in order to extract the dielectric function of

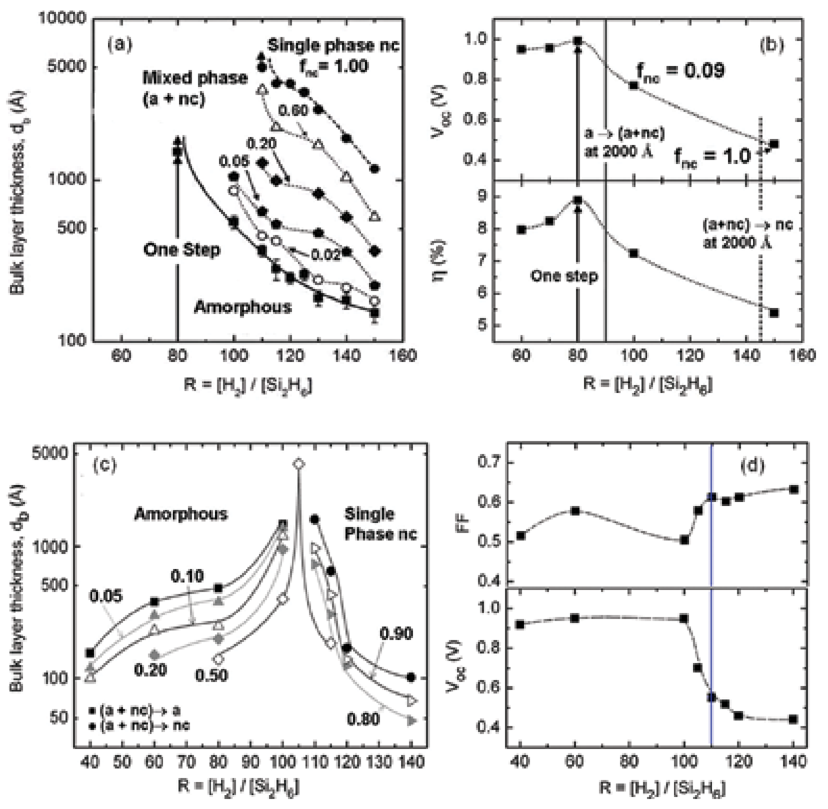

Figure 4. Deposition phase diagram (a) for a Si:H *i*-layers deposited on top of purely a-Si:H *n*-layers in the *n-i-p* configuration used for a-Si:H solar cells (contours on the diagram indicate f_{nc} values); (b) V_{oc} and efficiency versus the Si:H *i*-layer *R* value for single-junction solar cells [18]. Figure 4 (c) shows a deposition phase diagram for Si:H *i*-layers on nc-Si:H *n*-layer substrate films. These *i*-layers are designed for incorporation into nc-Si:H solar cells [18] (contours on the diagram indicate f_{nc} values); (d) V_{oc} and FF versus *R* for intended nc-Si:H solar cells in which case nc-Si:H *n*-layers are used. The vertical line identifies the optimum nc-Si:H solar cell performance [18].

the top ~ 1nm. In this way, a depth profile in the volume fraction of nanocrystallites, f_{nc}, can be obtained by applying the Bruggeman effective medium approximation [16] to the deduced dielectric function assuming a microscopic mixture of fully amorphous and fully nanocrystalline phases. For this deposition, the Si:H *i*-layer film nucleates on the *n*-layer as amorphous Si:H, undergoes an amorphous-to-nanocrystalline transition after a thickness of ~ 10nm, and then becomes fully nanocrystalline after a thickness of ~ 100nm.

Similar depth profiles obtained as a function of *R* from *R* = 80 to 150 have been used to construct a deposition phase diagram for the PECVD films as in Fig. 4(a) [18]. In this case, the Si:H *i*-layer films grown on a-Si:H *n*-layer films remain amorphous throughout the first ~200nm of bulk layer growth when $R \leq 80$. For higher *R* ($R \geq 100$), the Si:H *i*-layer films initially nucleate as a-Si:H, but then undergo an amorphous-to-nanocrystalline transition at a thickness that shifts from above 200nm to lower thicknesses with increasing *R*. Performance parameters of single-junction solar cells fabricated using a thickness of ~ 200nm for the Si:H *i*-layer, and different *R* values are shown in Fig. 4(b) [18]. The optimum V_{oc} and efficiency for this series of cells occurs when *R* = 80, which is the maximum *R* value possible such that the *i*-layer remains fully amorphous throughout its thickness. For a larger value of *R* = 100, the fraction of nanocrystallites in the near-surface of the final *i*-layer is small (~0.09), but these nanocrystallites apparently degrade V_{oc} due to their presence at the *i-p* interface in the completed device. This concept of maximum hydrogen dilution developed by RTSE is being applied widely to optimize the efficiencies of a-Si:H solar cells [21]. RTSE has suggested extensions of this concept using multistep and continuously variable dilution ratios *R* for improvements over simple single-step processes.

Another deposition phase diagram determined by RTSE is shown in Fig. 4(c), in this case for Si:H *i*-layers which are deposited on intended nanocrystalline Si:H (nc-Si:H) *n*-layers at the same nominal temperature of 200°C [18]. This is the layer structure used for a standard nanocrystalline *n-i-p* solar cell, and the resulting diagram exhibits significantly different behaviour than that of the Si:H *i*-layers on a-Si:H *n*-layers shown in Fig. 4(a). Initial stage mixed-phase Si:H growth results from a template effect due to the underlying nc-Si:H *n*-layer, which is itself mixed-phase, consisting of ~ 0.5/0.5vol. fraction ratio of a-Si:H/nc-Si:H. At lower dilution levels (*R* < 105), the mixed-phase *i*-layers evolve to a-Si:H due to a preference for amorphous growth. In this range of *R*, the mixed-phase nanocrystalline to amorphous [(a+nc) → a] transition shifts to larger thickness with increasing *R*. At higher dilution levels (*R* > 105), the initial mixed-phase material rapidly evolves to fully nc-Si:H due to the strong preference for nanocrystalline growth. In this range, the (a+nc) → nc transition shifts to lower thickness with increasing *R*. Fig. 4(c) reveals a bifurcation value of *R*=105, which divides the ultimate phase of the film between fully amorphous and fully nanocrystalline, even though the film nucleates as mixed-phase Si:H independent of *R*.

In the case of relatively thin 0.4–0.6μm nc-Si:H *i*-layers used in solar cells with performance shown in Fig. 4(d), the optimum one-step deposition process occurs on the basis of the phase diagram at the minimal value of *R* = 110, i.e., the smallest *R* value possible such that the *i*-layer evolves to dominantly nc-Si:H during its growth [18]. At *R* = 100 the (a+nc) → a transition occurs at a thickness of 150nm, and it is clear from the V_{oc} value of 0.95V in Fig. 4(d) that the top of the film is a-Si:H. At *R* = 120 the (a+nc) → nc transition occurs at a thickness of 20nm, and in this case, it is clear from the V_{oc} value of 0.46V that the top of the film is nc-Si:H. The highest performance nc-Si:H i-layer in Fig. 4(d) is observed at *R* =110, just before a more rapid drop in fill factor associated with the bifurcation region. For a higher substrate temperature, in which case the maximum nc-Si:H solar cell fill factor is larger, the rapid drop is even more dramatic. The continued lower fill factor for the low *R* Si:H films in Fig. 4(d) relative to those of Fig. 4(b) is attributed to the nc-Si:H phase at the bottom of the *i*-layer (about 40nm-thick for *R* = 60). Overall, these results demonstrate clear correlations between structural evolution from RTSE and solar cell performance that enable single-step, multi-step, and graded layer optimization.

CdTe

CdTe is used widely in thin-film photovoltaics as a *p*-type semiconductor serving as the active layer, along with CdS as its *n*-type heterojunction partner serving as a window layer. Thin films of CdTe can be produced by several different methods including vapour transport deposition (VTD), close-space sublimation (CSS), and rf magnetron sputtering [23]. The work reviewed here focuses on the use of RTSE to study thin films deposited by magnetron sputtering [24]. Although the sputter deposition rates of CdTe are generally slower, this deposition method is of interest because it allows one to fabricate efficient solar cell devices in a relatively low temperature process, limited by the temperature of the post-deposition treatment (~ 400°C). Also, by controlling sputtering parameters such as the temperature, pressure, and power, the growth mechanisms can be controlled, including the surface mobility of the deposited species, the bombardment energy and directionality of incident species, and the deposition rate/kinetics, respectively. These mechanisms determine the nano/microstructure of the sputter-deposited film [25, 26].

Fig. 5(a) shows the dielectric functions for bulk single crystal CdTe (c-CdTe) and an as-deposited polycrystalline CdTe film sputtered to 100nm thickness at 188°C [19]. Fig. 5(b) compares the room temperature dielectric functions of polycrystalline CdS films 50nm-thick fabricated at substrate temperatures of 145°C and 310°C [19]. All thin-film measurements were performed at room temperature by in-situ spectroscopic ellipsometry under vacuum before exposure of the freshly-deposited film to laboratory air. CdTe exhibits four critical points (CPs) over the energy range of $0.75 < E < 6.5$eV and CdS exhibits three CPs. In general, the CP amplitudes depend on the density of the material, the CP energies depend on the strain and the measurement temperature, and the CP widths depend on the grain size and measurement temperature. The lowest-energy CP, denoted E_0, represents the fundamental bandgap. For CdTe, the very broad dielectric function features for the thin film relative to c-CdTe are due to its fine grained structure. The blue-shifted E_0 energy for the polycrystalline CdTe film relative to c-CdTe is due to strain in the film. In addition, from the results for CdS, one can conclude that the grain size of this material increases with increasing substrate temperature.

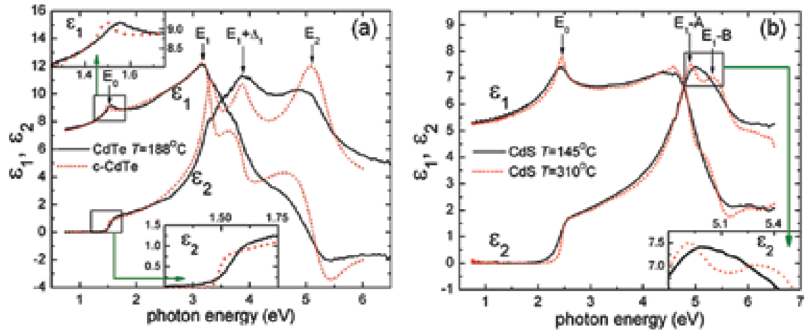

Figure 5. (a) Comparison of the room temperature dielectric function of an as-deposited polycrystalline CdTe thin-film magnetron sputtered at 188°C with that of c-CdTe [19]; (b) comparison of the room temperature dielectric functions of polycrystalline CdS thin films magnetron sputtered at 145°C and 310°C [19].

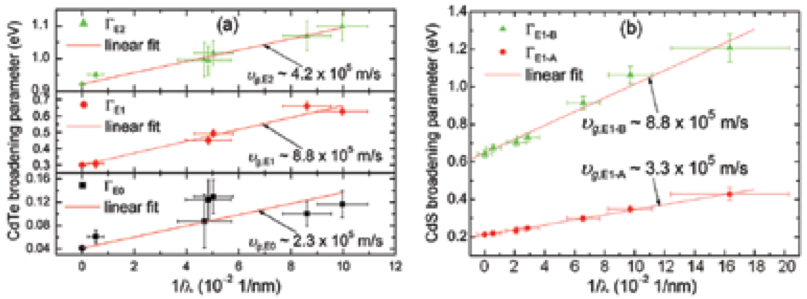

Figure 6. Broadening parameters plotted as functions of the reciprocal of the deduced mean free path for (a) CdTe and (b) CdS. The group speeds of excited carriers are calculated from the slopes of the linear fits using Equation 2 [19]. The poorer linearity for the CdTe E_0 is due to the large penetration depth, which leads to an averaging of the film structure at different depths.

The effects due to strain and grain size can be quantified by modelling the dielectric function as a sum of direct interband resonances at the band structure CPs using the parabolic band approximation with Lorentzian broadening. The *n*th CP generates the following lineshape in the complex dielectric function ε [13,22,27,28]:

$$\varepsilon(E) = A_n \exp(i\phi_n)\,[E - E_{0n} + i(\Gamma_n/2)]^{\mu n}, \quad (1)$$

where *E* is the photon energy, A_n is the *n*th CP amplitude, E_{0n} is the associated CP energy, Γ_n is the broadening energy, ϕ_n is the phase, and μ_n is the exponent. Considering as an example, a sample-dependent grain radius *R*, which controls the mean free path λ of the excited carriers associated with the *n*th CP, the following applies:

$$\Gamma_n = \Gamma_b + (h\nu_n/\lambda), \quad (2)$$

where $\lambda \sim R$ as a result of grain boundary scattering [19]. This expression is derived from the energy-time uncertainty principle, such that Γ_b is the single crystal CdTe broadening parameter, *h* is Planck's constant, and ν_n is the group speed of the excited carriers. The mean free path λ can be extracted from the Γ_n values for the dominant CPs of CdTe and CdS, using estimates of ν_n for these CPs derived from the band structure. Then, the other Γ_n values can be plotted versus 1/λ to evaluate the validity of the above relationship [19].

The results for the CPs of CdTe and CdS for two sets of samples fabricated at different substrate temperatures are shown in Fig. 6(a) and (b), respectively [19]. The points at 1/λ = 0 for CdTe are results for c-CdTe, and the nearby point is a $CdCl_2$ treated CdTe thin film. The linearity of the data for each of the higher energy critical points demonstrates consistency with Equation 2. These results have two implications: (i) that a meaningful mean free path can be extracted from the full set of CP broadening parameters for a given CdTe or CdS thin-film material; and

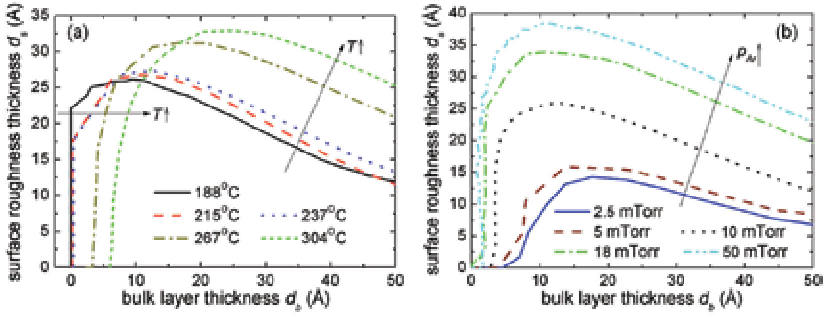

Figure 7. (a) Surface roughness evolution for CdTe thin films sputtered at different substrate temperatures [29]; (b) surface roughness evolution for CdTe thin films sputtered at different Ar pressures [30].

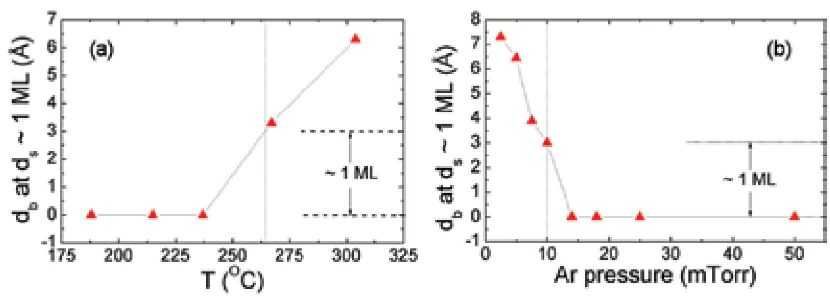

Figure 8. Bulk layer thickness d_b at a surface roughness layer thickness d_s of 1ML for CdTe thin films sputtered at different (a) temperatures and (b) Ar pressures.

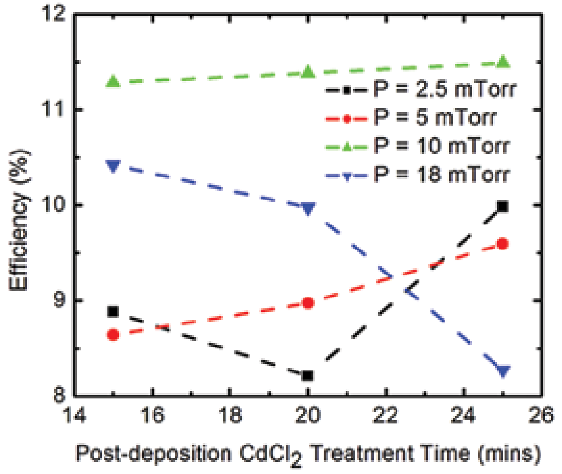

Figure 9. Efficiency of CdTe solar cells prepared at different Ar pressures as a function of the post-deposition CdCl$_2$ treatment time [30].

(ii) that in modelling dielectric functions of either CdTe or CdS, and accounting for their dependences on processing, one can replace the full set of broadening parameters Γ_n by a single mean free path that controls all of them, once the appropriate group speeds are available. For CdTe, for example, this reduces by three the number of lineshape parameters needed to model the dielectric function. A similar approach can be used to model strain, in which case each critical point energy E_{on} is controlled by strain, again reducing the number of lineshape parameters by three.

In further RTSE analyses of CdTe thin films, the nucleation and growth dynamics have been characterized as a function of the substrate temperature T and Ar pressure p_{Ar} [29,30]. These films were deposited onto silicon wafers covered with native SiO$_2$ due to their smoothness, reproducibility and well-known optical properties. Figs. 7(a) and 7(b) show the surface roughness thickness evolution for the temperature and pressure series, respectively, for the first ~ 5nm of growth [30]. In this case, for T < 267°C and for p_{Ar} >10mTorr, it is clear that surface roughness develops before a bulk-like layer is formed, which can be interpreted in terms of initial cluster growth, followed by bulk-like layer growth. In contrast, for T ≥ 267°C and p_{Ar} ≤ 10mTorr, a thin bulk-like layer is formed before surface roughness starts to develop, interpreted in terms of initial layer growth followed by cluster growth. These different initial growth modes are more pronounced when viewing plots of the bulk-like layer thickness at a cluster layer thickness of ~ 1 monolayer (ML), as shown in Figs. 8(a) and 8(b) for the temperature and pressure series, respectively.

These results from RTSE were also considered in view of CdTe solar cell performance. Thus, several devices were produced at different CdTe Ar pressures [30]. Each device underwent CdCl$_2$ post-deposition treatment for times ranging from 15 to 25 minutes and the resulting efficiency for each device is shown in Fig. 9. This figure shows that films deposited at low pressure appear to require longer treatment times for higher efficiency, whereas films deposited at high pressure (p_{Ar} = 18mTorr) appear to require shorter times. The best devices were obtained for p_{Ar} = 10mTorr, where the efficiency is not strongly dependent on treatment time. It has been suggested that this pressure is consistent with the transition in initial growth mode as observed by RTSE, and that a microstructure for optimum CdCl$_2$ treatment may be obtained in this transition region.

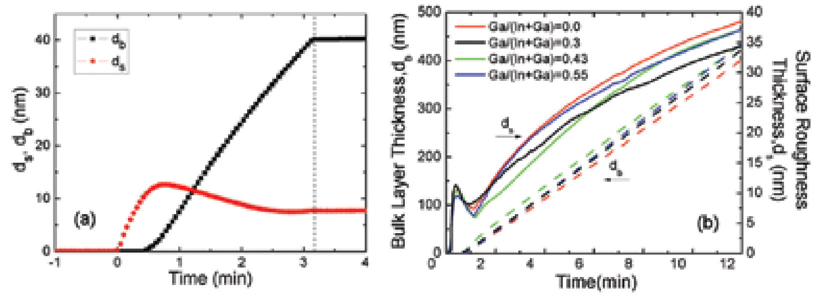

Figure 10. (a) Time evolution of surface roughness layer thickness d_s and bulk layer thickness d_b in the initial stages of growth for a thin CuInSe$_2$ film; (b) similar results over a wider time range highlighting the surface roughening for CIS as well as for CIGS with x = 0.30, 0.43 and 0.55. In (b) the solid lines correspond to d_s and the broken lines to d_b.

CIGS

The I-III-VI$_2$ chalcopyrite alloy system Cu(In$_{1-x}$Ga$_x$)Se$_2$ (CIGS) and related absorber material systems represent one of the most promising second-generation thin-film technologies for photovoltaic applications [31]. The very rough surfaces of such thin films at the thicknesses (1–2µm) used in photovoltaic devices imply that optical analysis can be challenging due to the reduction in irradiance of specularly transmitted and reflected light beams via scattering. Because the surface roughness increases in thickness during film growth, one way to avoid this problem is to perform measurements during film growth and to extract the dielectric function at a bulk layer thickness in the range of ~ 40–100nm. In general, such an approach enables an accurate surface roughness correction and avoids post-deposition oxidation, as well. This general approach was also utilized to obtain the dielectric functions for the CdTe and CdS films in Fig. 5 of the previous subsection. Such high accuracy dielectric functions deduced versus measurement temperature using this methodology can be expected to serve in future RTSE analyses, not only for analyzing the growth dynamics of alloy layers as in this article, but also for on-line monitoring in a manufacturing environment.

The CIS and CIGS thin films studied here were grown by codeposition on

Si(100) substrates held at a temperature in the range from 550 to 570°C. The CIS exhibited an average composition of Cu = 22%, In = 23%, and Se = 55%, a total thickness of ~50nm, a root mean square surface roughness of ~10nm, and a single α-phase with a slight preference in (112) orientation, as reported by a variety of *ex situ* measurements.

Fig. 10(a) shows the typical time evolution of both the surface roughness layer thickness (d_s) and the bulk layer thickness (d_b) deduced from RTSE data collected in the initial stages of the growth of a thin CIS film [32]. The Cu, In and Se shutters were opened and closed simultaneously at time zero and after 3.2 minutes of codeposition, respectively. Initial growth of the film is observed in the form of islands which increase to 11nm in thickness before the onset of bulk layer growth. The islands continue to grow until the onset of coalescence, as indicated by a decrease in d_s with an associated more rapid increase in d_b. Thereafter the film continues to smoothen as d_b increases approximately linearly with an average rate of 15nm/minute until shutter closure (dashed vertical line). The final values of surface roughness (d_s = 7.7nm) and total thickness ($d_b + d_s$ = 47.9nm) are in good agreement with those from *ex-situ* measurements. A weak upturn in d_s visible near three minutes in Fig. 10(a) represents the onset of roughening which is explored in greater detail in Fig. 10(b). This latter figure shows corresponding results over a longer time duration for CIS and CIGS with x = 0.30, 0.43, and 0.55.

For each deposition in Fig. 10(b), the dielectric functions of the bulk layer can be determined at the deposition temperature. As an example, dielectric functions of the CIS bulk layer of Fig. 10(a) are shown in Fig. 11(a). Two representative results are displayed; one was obtained from real-time data acquired at the growth temperature of 550°C whereas the other was obtained from data acquired *in-situ* after cooling to 20°C. For further interpretation of these dielectric functions, an optical averaging effect in the polycrystalline films may be taken into account due to the anisotropy of single-crystal CIS [33-37]. Given the uniaxial nature of the tetragonal chalcopyrite crystal structure of CIS and the lack of a strong orientation of the studied films, however, it is expected that the dielectric functions of Fig. 11(a) more closely resemble the ordinary component of the single crystal dielectric function [34].

A comparison of the results in Fig. 11(a) reveals characteristic red shifts of the CP energies and increases in CP broadening parameters with increasing temperature. These can be quantified by modelling each of the dielectric functions as a sum of direct interband resonances at the band structure CPs according to Equation 1. A sum of up to 12 CPs was used to simulate the convolved dielectric functions of the polycrystalline CIS thin films along the ordinary and extraordinary rays. The CP energies obtained with such fits were found to agree well with results reported for single crystals [33], whereas three high-energy transitions at 5.11, 5.41 and 5.91eV have been identified for the first time in the RTSE study. With the availability of 12 CP energies, it may be possible in the future to track composition, sample temperature and possibly strain from the RTSE data, assuming the appropriate database components have been established.

Due to the complexity of the CIGS material system as well as the solar cell stack itself, many other opportunities exist for RTSE in the evaluation and possible control of the CIGS growth processes. For example, Fig. 11(b) (lower panel) compares the imaginary parts of the dielectric functions of a CIGS layer extracted at various times for a thin film grown by a two-stage process from a Cu-rich film to a Cu-poor film. Fig. 11(b) (upper panel) shows corresponding results for a CIGS film grown from Cu-poor to Cu-rich. Below the onset of the band gap in both cases, the magnitude of the imaginary part of the dielectric function ε_{2f} scales with Cu content [38]. Thus in a transition from Cu-rich to Cu-poor, there is a monotonic decrease in ε_{2f} below the band gap. This effect is the result of a decrease in free carrier concentration which can be modelled with a Drude contribution to the dielectric function, given by:

$$\varepsilon = -A_D^2 (E^2 + i\Gamma_D E)^{-1} \qquad (3)$$

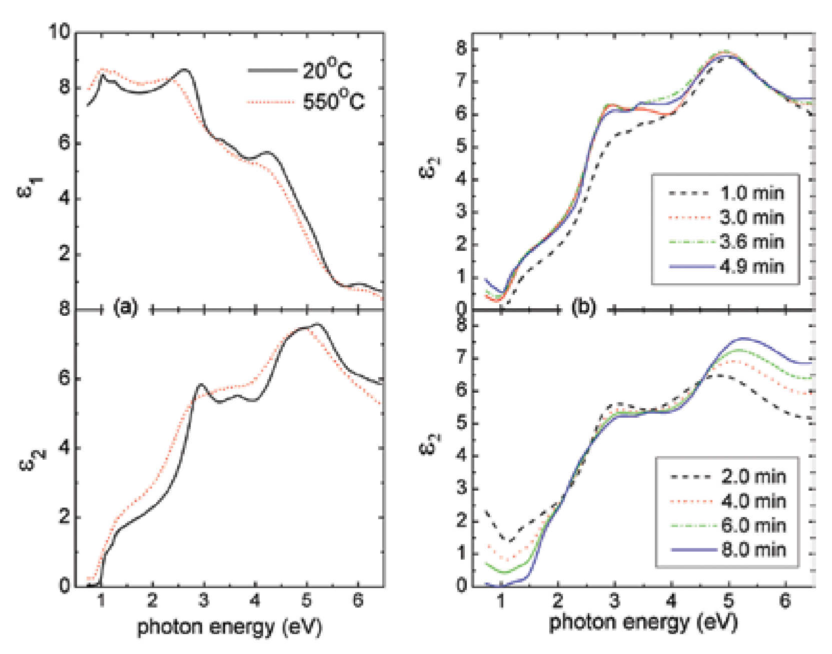

Figure 11. (a) CIS bulk layer dielectric functions at 550°C and 20°C; (b)the imaginary parts of the dielectric functions of a CIGS layer extracted at various times for a thin film grown by a two-stage process from a Cu-rich film to a Cu-poor film (lower panel); results for a CIGS film grown from Cu-poor to Cu-rich (upper panel) [38].

where A_D and Γ_D are Drude amplitude and broadening parameters. The free electrons in Cu-rich CIGS film are suspected to arise from a conducting $Cu_{2-x}Se$ semimetal phase at the grain boundaries and on the surface [39]. The presence of a conductive phase was also confirmed at the end of the deposition by a sheet resistance measurement, which was $5k\Omega/\square$ for the Cu-rich films of Fig. 11(b) (top panel) and $70M\Omega/\square$ for the Cu-poor films of Fig. 11(b) bottom panel [38]. Although the magnitude of these ε_{2f} variations appear small in Fig. 11(b), the large thickness of film amplifies the effect in the (ψ, Δ) data, leading to the ability to control the Cu content simply on the basis of the RTSE output versus time at low energy.

The Cu-poor films of Fig. 11(b) (bottom) were grown after a Cu-rich phase, whereas the Cu-poor films of Fig. 11(b) (top) were grown before the Cu-rich phase, with an initial growth comparable to a one-stage process [38]. Determination of Γ_n values show that films that are Cu-poor at the end of the deposition (Fig. 11(b), bottom) have a longer mean free path than those that are Cu-rich at the end of the deposition (Fig. 11(b), top). XRD measurements and AFM images taken after film growth reveal a larger grain size for the final films that are Cu-poor. Thus, the longer mean free path determined for those films reflects the process of grain boundary scattering, and demonstrates that the CP widths are providing key processing information towards optimum CIGS materials for device applications.

Summary and future directions

Polarization spectroscopies, in particular optical methods based on spectroscopic ellipsometry, are becoming increasingly popular as the interest in developing, optimizing and scaling up thin-film photovoltaic devices has grown. Real-time spectroscopic ellipsometry (RTSE) allows one to study the characteristics of thin-film growth processes ranging from the initial nucleation and coalescence stage to the final film structural depth profile. A sampling of information that can be extracted from RTSE has been provided in this article and includes: (i) phase diagrams that can guide optimization in the case of Si:H thin films; (ii) material quality and growth mode determination in the case of CdTe thin films; and (iii) Cu content and final material quality in the case of CIGS thin films. These examples provide insights into why solar cells deposited under different conditions result in varying efficiencies, and overall, they help in process development for thin films deposited by different techniques including plasma-enhanced chemical vapour deposition, magnetron sputtering and multi-source evaporation.

As shown in this article, RTSE is well established for the characterization of thin-film photovoltaic materials in a research and development environment; however, excellent prospects also exist for expansion to the pilot and full-scale production environments. For example, RTSE can be applied to monitor solar cell fabrication on flexible substrates in roll-to-roll processes. In this case, one can track the initial start-up of the deposition process and the stability at a particular thickness point in the process. Also, using a dielectric function database obtained from RTSE measurements, one can characterize completed solar devices *ex-situ* for relevant information such as component layer thicknesses and compositions. For superstrate modules deposited on glass, the glass/film-stack interface is generally smoother than the film back-side, and this motivates the technique of through-the-glass ellipsometry. The interest in studying large-area partially or fully completed modules from production lines motivates mapping spectroscopic ellipsometry, in which case thickness and compositional maps can provide insights into process uniformity.

Acknowledgments

The authors gratefully acknowledge support from DOE Grants No. DE-FG36-08GO18067 and DE-FG36-08GO18073 and from the State of Ohio Third Frontier's Wright Centres of Innovation Program. Prof. André Ferlauto, Prof. Nikolas Podraza, Dr. Vikash Ranjan, Dr. Simon Cao, Lila Dahal, Naba Paudel and Jason Stoke contributed to the research described herein.

References

[1] Luque, A. & and Hegedus, S. (eds.), 2003, *Handbook of Photovoltaic Science and Engineering*, John Wiley & Sons, Somerset, NJ.

[2] Herman, I. P. 1995, *Optical Diagnostics for Thin Film Processing*, Academic, New York.

[3] Azzam, R. M. A. & Bashara, N. M. 1977, *Ellipsometry and Polarized Light*, North-Holland, Amsterdam.

[4] Tompkins, H.G. 1992, *A User's Guide to Ellipsometry*, Academic, New York.

[5] Fujiwara, H. 2007, *Spectroscopic Ellipsometry: Principles and Applications*, John Wiley & Sons, West Sussex UK.

[6] Tompkins, H.G. & Irene, E.A. (eds.), 2005, *Handbook of Ellipsometry*, William Andrew, Norwich NY.

[7] (a) Boccara, A.C., Pickering, C. & Rivory, J. 1993 (eds.), *Proc. 1st ICSE*, Elsevier, Amsterdam (also published as Thin Solid Films, pp. 233–234).
(b) Collins, R.W., Aspnes, D.E & Irene, E.A. (eds.) 1998, *Proc. 2nd ICSE*, Elsevier, Amsterdam (also published as Thin Solid Films, pp. 313–314).
(c) Fried, M., Humlicek, J. & Hingerl, K. (eds.) 2003, *Proc. 3rd ICSE*, Elsevier, Amsterdam.
(d) Arwin, H., Beck, U. & Schubert, M. (eds.), 2007, *Proc. 4th ICSE*, Wiley-VCH, Weinheim, Germany.
(e) Tompkins, H.G. et al. (eds.) 2011, *Proc. 5th ICSE*, Elsevier, Amsterdam, in press.

[8] Aspnes, D.E. & Studna, A.A. 1975, "High precision scanning ellipsometer",

Appl. Opt. Vol. 14, pp. 220.

[9] (a) Palik, E.D. 1985, *Handbook of optical constants of solids*, Academic, New York.
(b) Palik, E.D. 1991, *Handbook of optical constants of solids II*, Academic, New York.

[10] Aspnes, D.E. 1976, "Spectroscopic ellipsometry", in Seraphin, B.O. (ed.), *Optical Properties of solids: new developments*, North-Holland, Amsterdam, p. 799.

[11] Collins, R.W. et al. 2005 "Multichannel ellipsometry", in Tompkins, H.G. and Irene, E.A. (eds.), *Handbook of ellipsometry*, William Andrew, Norwich NY, p. 481.

[12] Wooten, F. 1972, *Optical properties of solids*, Academic, New York.

[13] Collins, R.W. & Ferlauto, A.S. 2005, "Optical physics of materials", in Tompkins, H.G. & Irene, E.A. (eds.), *Handbook of ellipsometry*, William Andrew, Norwich NY, p. 93.

[14] Jellison, Jr., G.E. "Data analysis for spectroscopic ellipsometry", in Tompkins, H.G. & Irene, E.A. (eds.), 2005 *Handbook of ellipsometry*, William Andrew, Norwich, NY, p. 237.

[15] Aspnes, D.E. 1982, "Optical properties of thin films", *Thin Solid Films*, Vol. 89, p. 249.

[16] Fujiwara, H. et al. 2000, "Assessment of effective-medium theories in the analysis of nucleation and microscopic surface roughness evolution for semiconductor thin films", *Phys. Rev. B*, Vol. 61, p. 10832.

[17] Hauge, P. S.1980, "Recent developments in instrumentation in ellipsometry", *Surf. Sci.*, Vol. 96, p.108.

[18] Stoke, J.A. et al. 2008, "Optimization of Si:H multijunction n-i-p solar cells through the development of deposition phase diagrams", *Proc. 33rd IEEE PVSC*, New York, Art. p. 413.

[19] Li, J., Podraza, N.J. & Collins, R.W. 2007, "Real time spectroscopic ellipsometry of sputtered CdTe, CdS, and CdTe$_{1-x}$ S$_x$ thin films for photovoltaic applications", *Phys. Stat. Sol. (a)*, Vol. 205, p. 91.

[20] Deng, X. & Schiff, E.A. 2003, "Amorphous silicon-based solar cells" , in: A. Luque and S. Hegedus (eds.), *Handbook of photovoltaic science and engineering*, John Wiley & Sons, Somerset, New Jersey, p. 505.

[21] Collins, R.W. et al. 2003, "Evolution of microstructure and phase in amorphous, protocrystalline, and microcrystalline silicon studied by real-time spectroscopic ellipsometry", *Solar Energy Materials and Solar Cells*, Vol. 78, p.143.

[22] Lautenschlager, P. et al. 1987, "Temperature dependence of the dielectric function and interband critical points in silicon", *Phys. Rev. B*, Vol. 36, p. 4821.

[23] McCandless, B.E. & Sites, J.R. 2003 "Cadmium telluride solar cells", in Luque, A. & Hegedus, S. (eds.), *Handbook of Photovoltaic Science and Engineering*, John Wiley & Sons, Somerset, New Jersey, p. 617.

[24] Compaan, A.D. et al. 2009, "Magnetron sputtering for II-VI solar cells: thinning the CdTe", *Mat. Res. Soc. Symp. Proc.,* Paper M09-01, Vol. 1165, MRS, Warrendale, PA.

[25] Messier, R., Giri, A.P. & Roy, R.A. 1984 "Revised structure zone model for thin film physical structure", *J. Vac. Sci. Technol. A,* Vol. 2, p. 500.

[26] Mirica, E., Kowach, G. & Du, H. 2004, "Modified structure zone model to describe the morphological evolution of ZnO thin films deposited by reactive sputtering", *Crystal Growth and Design*, Vol. 4, No.157.

[27] Lautenschlager, P. et al. 1987, "Interband critical points of GaAs and their temperature dependence", *Phys. Rev. B*, Vol. 35, p. 9174.

[28] Aspnes, D.E., in Balkanski, M. (ed.) 1980, *Handbook on semiconductors*, North-Holland, Amsterdam, Vol. 2, Chap. 4A.

[29] Li, J. et al. 2006, "Real-time spectroscopic ellipsometry of sputtered CdTe: effect of growth temperature on structural and optical properties", *Proc. 4th World Conf. Photovolt. Energy Conv*, p. 392.

[30] Sestak, M.N. et al. 2009, "Real-time spectroscopic ellipsometry of sputtered CdTe thin films: effect of Ar pressure on structural evolution and photovoltaic performance", *Mat. Res. Soc. Symp. Proc.*, MRS, Warrendale PA, Vol. 1165, Paper M09-02.

[31] Repins, I. et al. 2008, "19.9%-efficient ZnO/CdS/CuInGaSe$_2$ solar cell with 81.2% fill factor", *Prog. Photovolt.*, Vol. 16, p. 235.

[32] An, I. et al. 1990, "Microstructural evolution of ultrathin amorphous silicon films by real time spectroscopic ellipsometry." *Phys. Rev. Lett.* Vol. 65, p. 2274.

[33] Alonso, M.I. et al. 2001, "Optical functions and electronic structure of CuInSe$_2$, CuGaSe$_2$, CuInS$_2$, and CuGaS$_2$", *Phys. Rev. B*, Vol. 63, p. 75203.

[34] Alonso, M.I. et al. 2000, "Optical properties of chalcopyrite CuAl$_x$In$_{1-x}$Se$_2$ alloys" *J. Appl. Phys.*, Vol. 88, p. 5796.

[35] Paulson, P.D., Birkmire, R.W. & Shafarman, W.N. 2003, "Optical characterization of CuIn$_{1-x}$Ga$_x$Se$_2$ alloy thin films by spectroscopic ellipsometry", *J. Appl. Phys.*, Vol. 94, p. 879.

[36] Kawashima, T. et al. 1998, "Optical constants of CuGaSe$_2$ and CuInSe$_2$", *J. Appl. Phys.*, Vol. 84, p. 5202.

[37] Kreuter, A. et al. 2001, "Anisotropic dielectric function spectra from single-crystal CuInSe$_2$ with orientation domains", *Appl. Phys. Lett.*, Vol. 78, p.195.

[38] Marsillac, S. Et al. 2008, "In-situ study of CIGS dielectric function as a function of copper content", *Proc. 35th IEEE PVSC*, p. 866.

[39] Schock, H.W. 2004, "Properties of chalcopyrite-based materials and film deposition for thin-film solar cells", Y. Hamakawa, (ed.), *Thin-film Solar Cells: Next Generation Photovoltaics and its Applications*, Springer, Berlin, p.163.

About the Authors

Dr. Robert W. Collins is a professor and NEG endowed chair in the department of physics and astronomy at the University of Toledo, Ohio. He co-directs the Center for Photovoltaics Innovation and Commercialization and has been involved in research and development of thin-film photovoltaics since 1976.

Dr. Jian Li received his Ph.D. from the University of Toledo, Ohio in 2010 and is currently a post-doctor at the National Renewable Energy Laboratory, Colorado. His research interests involve the development and application of spectroscopic ellipsometry.

Dr. Sylvain Marsillac is an associate professor in the department of electrical and computer engineering at Old Dominion University, Virginia. He specializes in the science and engineering of solar cell fabrication and characterization. He has authored more than 100 papers in peer-reviewed journals and conference proceedings.

Michelle N. Sestak is currently a doctoral student at the University of Toledo, Ohio. Her thesis research includes application of spectroscopic ellipsometry for the study of II-VI thin-film photovoltaic materials.

Enquiries

Center for Photovoltaics Innovation & Commercialization and Department of Physics & Astronomy, University of Toledo, Toledo, Ohio 43606, USA
Tel: +1 419 530 3843
Email: robert.collins@utoledo.edu

National Renewable Energy Laboratory,
1617 Cole Boulevard, Golden, Colorado, 80401, USA

Department of Electrical & Computer Engineering
Old Dominion University, Norfolk, Virginia 23529, USA